Atom probe analysis of Sn in Zr-based alloys

N. Sano *, K. Takeda

Corporate Research and Development Laboratories, Sumitomo Metal Industries Ltd., 1–8 Fuso-cho, Amagasaki 660, Japan

Abstract

We have extensively used atom-probe field ion microscopy (APFIM) for microanalyses of a heat-treated Zircaloy-4 and Zr–Sn alloys containing 0.6 or 1.39 wt% Sn and clarified as to whether Sn is fully dissolved or not in the α-Zr matrix. It is found that Sn dissolves in the matrix of both Zircaloy-4 and Zr–0.6 wt% Sn alloy upon annealing at 723 K. For Zr–1.39 wt% Sn alloy, after annealing for more than 200 h, the symptom of phase separation has been found. The distribution of Sn in the matrix is changed from the α-quenched state, and local regions enriched with Sn are formed in the matrix. © 1998 Elsevier Science B.V.

1. Introduction

Zirconium based alloys have been widely used for nuclear tubing materials in severe corrosive environments, such as in pressurized pure water steam at elevated temperatures. A small addition of Sn, Fe, Cr and/or Ni has been known to be effective to improve corrosion and oxidation resistance [1] so that commercial Zr alloys contain those alloying elements. Examples are Zr–1.5Sn–0.2Fe–0.1Cr (usually called Zircaloy-4), and Zr–1.5Sn–0.1Fe–0.1Cr–0.07Ni (Zircaloy-2). According to the binary phase diagram [2], as reproduced in Fig. 1, Sn can be dissolved in α-Zr up to about 9.3 wt%, but its solubility decreases sharply with decreasing temperature. In the course of fabrication process, Zr alloys experience a complicated thermomechanical treatment. Zircaloy-4 is subjected to the final annealing around 723 K, where the solubility of Sn is less than 1 wt%. Hence, intermetallic compounds of Sn are expected to precipitate in the α-Zr matrix during this treatment if the diffusion of Sn is sufficiently fast. In contrast to the precipitation of intermetallic compounds composed of Zr and Fe and/or Cr, Sn-rich precipitates

have never been well characterized. Meng and Northwood [3] have reported that Zr_4Sn precipitates associated with dislocation networks in Zircaloy-4 solution-treated at 1373 K then air-cooled. Kuwae et al. [4] have observed Zr_5Sn_3 and ZrSn precipitates in β-quenched Zircaloy-2, though the latter precipitates are not expected in the equilibrium binary phase diagram [2]. Bangaru [5] has reported that Sn tends to segregate at lath boundaries and grain boundaries in β-quenched Zircaloy-4, although the concentration of Sn becomes quite uniform after annealing in the α phase region. Recently, Aihara et al. [6] have claimed based on their TEM observations that very small (< 10 nm) Zr_4Sn particles homogeneously precipitate in Zircaloy-4 and Zr–1.5 wt% Sn binary alloys. Using atom probe field ion microscopy (APFIM), Andrén et al. [7–11] have measured the chemical composition of surface oxide films and that of the matrix in heat-treated Zircaloy-4. Although they obtained no large clean surfaces upon APFIM analysis due to the difficulty of removing sticky oxide film formed on a needle-shaped specimen, an almost equal amount of Sn to the nominal composition was detected from the matrix of the Zircaloy-4 finally annealed at around 773 K. Kruger et al. [12] have analyzed Zircaloy-2 by APFIM. Although the final annealing was performed at higher temperature of 873 K for 2 h, Sn concentrations in the matrix determined by APFIM were found to be comparable to the nominal

---

* Corresponding author. Tel.: +81-6 489 5756; fax: +81-6 489 5960; e-mail: sano@pca.amaken.sumikin.co.jp.
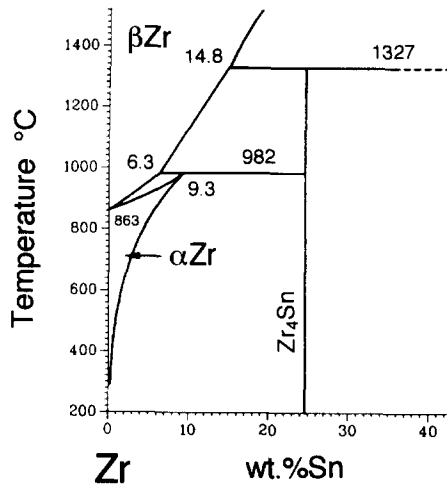
Fig. 1. Zr-rich side of a Zr–Sn binary alloy phase diagram [2].

reduction ratio of 50%. After these thermomechanical treatments, sample A (Zr–0.65Sn–0.19Fe–0.10Cr alloy) and sample B (Zircaloy-4) were subsequently annealed at 1053 K for 2 h, followed by a 50% cold rolling, then finally annealed at 723 K for 2.5 h. Other samples, namely C (Zr–0.60Sn alloy) and D (Zr–1.39Sn alloy), were subsequently annealed at 1073 K for 1 h, followed by an oil-quench at room temperature (α-quench), then subjected to the final annealing at 723 K for various periods of time up to 211 h. The square rods of approximately 1 mm $\times$ 1 mm $\times$ 10 mm were cut from the heat treated samples, then electrolytically polished to needle-shaped APFIM specimens using a solution of 90 vol.% acetic acid and 10 vol.% perchrolic acid. At the final stage of electropolishing, the polishing time was carefully controlled, otherwise thick oxide films quickly formed on the specimen surface. The electropolished specimens were thoroughly rinsed only in methanol and quickly transferred to a vacuum chamber of an APFIM. The APFIM used in this study is a conventional energy-compensated ToF type equipped with a Poschenrieder electrostatic lens, with the flight distance of 2500 mm. The mass resolution, $m/\Delta m$, of this instrument is over 500, where m is the atomic number and Δm is the full width at half maximum (FWHM) at m. A typical mass histogram of sample A is shown in Fig. 2, where the number of detected ions is plotted against mass-to-charge ratio, m/n, where n is the charge state of ions. In APFIM analyses, ions are detected not only as single charged particles ($n = 1$), but also multiply charged ones ($n \geq 2$). The charge state of ions is affected by many factors, but mainly depends on the analyzing voltage and mass of ions. In the present study, most of Zr ions were detected as doubly or triply charged ions. Each element and isotopes of Zr are clearly distinguished in Fig. 2 so that the mass resolution of the instrument is high enough for the present study.

alloy compositions. As mentioned above, experimental results are contradictory to each other and it is still unclear whether Sn is precipitated or fully dissolved in the α-Zr matrix. Hence, we have performed APFIM analyses of heat-treated Zircaloy-4 and Zr–Sn alloys containing 0.6 or 1.39 wt% Sn, all of which are finally annealed at 723 K for various periods of time. Since APFIM is based on the measurement of the time-of-flight (ToF) of individual ions, it provides the equal detection efficiency for all the elements. This technique is also quite powerful for analyzing the small amount of alloying elements in local regions, if the statistically sufficient number of ions is collected. We have successfully prepared APFIM specimens bearing a larger clean surface to allow detailed observations of FIM images and statistically reliable chemical analysis of the matrix. Our results have shown that Sn remains dissolved in the matrix both of Zircaloy-4, which is subjected to the conventional thermomechanical treatment, and of Zr–0.6 wt% Sn alloy, which is annealed at 723 K up to 200 h. For Zr–1.39 wt% Sn alloy, after annealing for more than 200 h, the symptom of phase separation has been found. The distribution of Sn in the matrix is changed from the α-quenched state, and local regions enriched with Sn are formed in the matrix.

The atom probe analyses were performed at 90 K under 1×10^{-5} Pa Ne with the pulse fraction of 17 to 20%. This condition was not optimal so the accuracy of measured concentrations of Sn was slightly deteriorated. Analyses at lower temperatures, however, frequently resulted in specimen rupture during the analyses and it was very difficult to collect a large number of ions which was necessary for statistically reliable analyses. However, the experimental

2. Experimental

In the present study, Zircaloy-4 and three kinds of Zr–Sn alloys are investigated. Their chemical compositions are given in Table 1. All the alloys were commonly subjected to the thermomechanical treatment; that is, (1) solution-treated at 1323 K for 1 h followed by an oil-quench at room temperature (β-quench), (2) hot rolled with the reduction ratio of 60% at 923 K followed by an intermediate annealing at 923 K for 1 h, (3) cold rolled with the

Table 1
Chemical composition (wt%) of Zr based alloys used in the present study

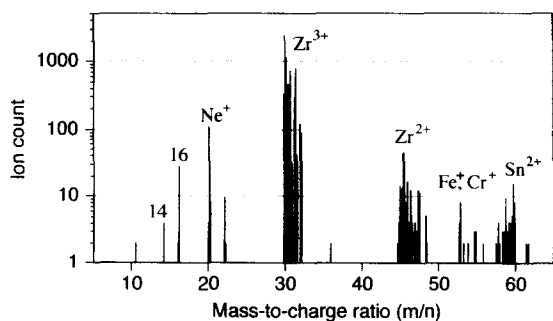| Sample	Sn	Fe	Cr	N	Zr
A	0.65	0.19	0.10	0.0040	bal.
B	1.41	0.19	0.10	0.0036	bal.
C	0.60	–	–	0.0007	bal.
D	1.39	–	–	0.0007	bal.

Fig. 2. A mass histogram of sample A (Zr–0.65Sn–0.19Fe–0.10Cr).

conditions were identical for all the samples to allow data comparisons so that the change of Sn concentration in the matrix could be determined, and nm-sized particles in the matrix could be observed in FIM images. The FIM images were observed using Ne gas. Since an image contrast of precipitates is known to be affected by temperatures, the specimen temperature was changed through 90 to 50 K during observations not to miss the presence of the precipitates. Hardness change upon annealing at 723 K was measured on sheet materials 1 mm in thickness using a micro-Vickers hardness tester with a load of 50 g by averaging six readings for each annealing condition.

3. Results and discussion

Fig. 3 shows an FIM image of sample A (Zr–0.65Sn–0.19Fe–0.10Cr finally annealed at 723 K for 2.5 h) showing the arrangement of concentric rings of a clean surface which are Miller-indexed based on the hcp structure. Each bright dot composing concentric rings is an individual atom and an innermost ring is the peripheral of the topmost layer of the locally faceted surfaces at the apex of the needle-shaped specimen. Image contrast is uniform throughout the surface and no precipitates with brighter or darker contrast against the matrix are observed. Sample A contains less Sn, namely 0.65 wt%, then it is probable that all the Sn could completely dissolve into the matrix at 723 K. During FIM observations, successive field evaporation of surface layers of the needle-shaped specimen exhibits the interior of the bulk. As field evaporation proceeds, the curvature of the apex of the specimen increases, namely the needle becomes blunter. However, the applied voltage cannot be increased over 30 kV due to instrumental limitations, so we can only observe a limited volume of the bulk region. Generally, observable volume in a single trial of FIM specimen is about 100 nm in diameter and about a few hundreds of nanometer at maximum in depth direction (parallel to the specimen axis). Therefore, if nanometer-sized precipitates are homogeneously distributed with the average interparticle distance less than about 100 nm or

with the sufficient number density, a part of precipitation (at least a single precipitate particle) can be detected by FIM observations. This kind of critical situations has been simulated by assuming needle-shaped space into which spherical particles with various diameters and number densities are randomly distributed [13]. Fig. 4 shows a typical simulation result [13], where the anticipated number to be observed of spherical precipitates with varying diameters during an FIM observation using a single specimen is plotted against the number density of precipitates. It shows that the critical number density below which no precipitation may be detected is approximately 3×10^{16} cm^{-3} with the precipitate diameter as small as 2 nm. During the course of the present study, we observed more than 30 specimens fabricated from sample B with a higher Sn content (Zircaloy-4 finally annealed at 723 K for 2.5 h), but it was only one time that we discovered the Sn-rich precipitate. Therefore, it is not likely that nanometer-sized Sn-rich particles precipitate homogeneously in the matrix of the Zircaloy-4, as claimed by Aihara et al. [6]. We have also measured the Sn concentration in the matrix of sample B. Fig. 5 presents an integrated depth profile taken from the matrix region of sample B. In this kind of representation of APFIM data, the cumulative number of solute ions (Sn, Fe and Cr) is plotted against the cumulative number of total ions (a sum of solute and solvent ions, or, Sn + Fe + Cr + Zr), and a local slope of each curve corresponds to a local concentration of respective solute elements. Ions are collected through a small aperture called probe hole, which is seen as a dark circle (indicated by an arrow) located at the center of the FIM image shown in Fig. 3. A projected diameter of the probe hole on the specimen surface is dependent on the curvature of the apex of the
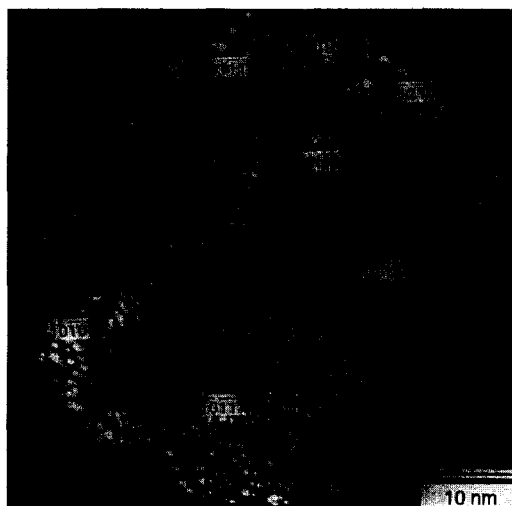

Fig. 3. A Ne field ion image of sample A. Numbers shown in the figure are Miller indices for the hcp structure. A dark circle in the center of the image (indicated by an arrow) is a probe hole.
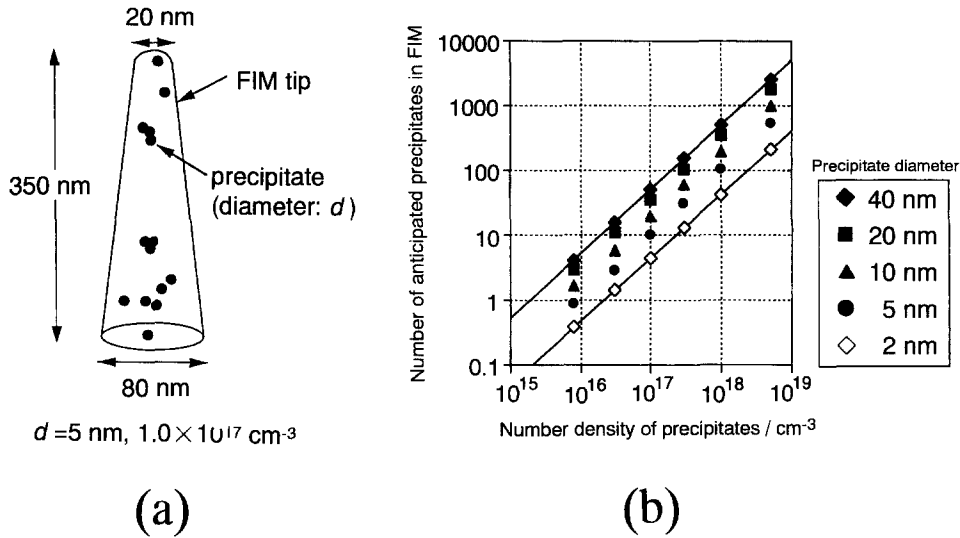
Fig. 4. (a) A simulated needle-shaped specimen containing spherical precipitates, and (b) the anticipated number of precipitates to be observed during an FIM observation using a single specimen.

specimen, namely dependent on the analyzing voltage. In the present study, the projected diameter was estimated to be about 1 to 2 nm so that the probe hole covered 30 to 100 ions per 'surface layer'. Thus, the x-axis of Fig. 5 can be translated to the number of the surface layers sequentially removed from the beginning of the APFIM analysis. The thickness of this surface layer depends on the crystallographic orientations so that it is difficult to precisely evaluate the absolute depth distance of analyzed volume unless the probe hole is adjusted right on a specific crystallographic pole. In the present study we have located the probe hole around high Miller index poles in order to collect more ions in shorter periods of time. The average coverage of the probe hole is supposed to be 60 ions per surface layer and its thickness is assumed to be 0.32 nm (the lattice parameter of the a axis of α-Zr); thus, the maximum of the x-axis of Fig. 5 corresponds to about 85 nm. In Fig. 5, Sn is detected continuously (namely, the slope of Sn is uniform), at least in the range of distance about 85 nm. Average Sn concentration, C, is determined

to be $1.31 \pm \sigma$ ($\sigma = 0.09$) at.% (1.68 ± 0.13 wt%). The statistical error, σ, is calculated by the following relationship,

$$\sigma = \sqrt{\frac{C(1-C)}{N}} \, , \qquad (1)$$

where N is the total number of ions detected. Although the average Sn concentration appears slightly higher than the nominal alloy composition due to the higher specimen temperature, no local depletion or enrichment of Sn in the matrix is found, which indicates that Sn is dissolved in the matrix.

As mentioned above, the Sn-rich precipitate was actually observed although it appeared to be rare in a submicron scale. Fig. 6 shows an FIM image of the Sn-rich precipitates (brighter region) found in sample B, whose diameter is approximately 20 nm. Inside the precipitate, ring structures of bright dots are observed, indicating that
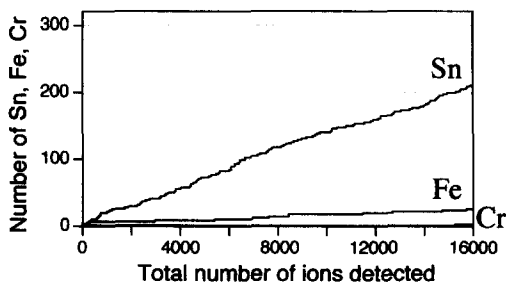

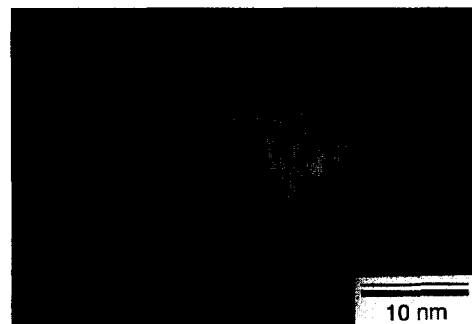Fig. 5. An integrated depth profile of a matrix region of sample B (Zircaloy-4).

Fig. 6. A Ne field ion image of a very rare Sn-rich precipitate discovered in sample B (Zircaloy-4).

the precipitate has an ordered structure (characteristic of an intermetallic compound). Its chemical composition determined from the APFIM analysis is Zr–(45 ± 5.0) at.% Sn. This value is closer to the Sn concentration of Zr_5Sn_3 or ZrSn precipitates than to that of Zr_4Sn which is expected to precipitate upon annealing at 723 K. Associated with the fact that the size of this precipitate is relatively large (about 20 nm in diameter), we believe that this precipitate has not formed during the isothermal annealing at 723 K, rather it was formed during the prior thermomechanical treatment or even during the solidification stage, and remained undissolved.

According to a note associated with the Zr–Sn binary phase diagram [2], even a small amount of iron makes the Zr_4Sn unstable, then it may be possible that iron deters the precipitation of Zr_4Sn or some part of these precipitates may have dissolved again into the matrix during annealing at 723 K. In order to avoid the aforementioned effect of iron, we have studied the Zr–1.39 wt% Sn binary alloy free from iron and chromium. Using the diffusion data for Sn in α-Zr, we can estimate the diffusion distance of Sn

and evaluate precipitation kinetics at 723 K. However, the diffusion of Sn in α-Zr has been measured only at higher temperature regions (> 973 K) [14], so the available data may not be compatible for estimating the diffusion distance at 723 K. By assuming the same pre-exponential factor and activation energy as for > 973 K ($D = 2.22 \times 10^{-19}$ m^2/s [14]), the diffusion distance x ($= \sqrt{Dt}$) of Sn at 723 K for 200 h is estimated to be approximately 400 nm. If Sn atoms could actually move as long as 400 nm, Zr_4Sn particles might precipitate from the supersaturated matrix, because their size is about a few nm and their inter-particle distance is less than a few hundred nm. Fig. 7 shows the FIM images and concentration depth profiles for sample D which were α-quenched (namely solution-treated in α field followed by an oil-quenching), and annealed at 723 K for 211 h. The concentration depth profile is another typical representation of APFIM data, where the cumulative number of total ions is divided into blocks and solute concentration is calculated for each block. In this kind of plot, the variation of solute concentration along the depth direction in the bulk is visualized. The number of ions per
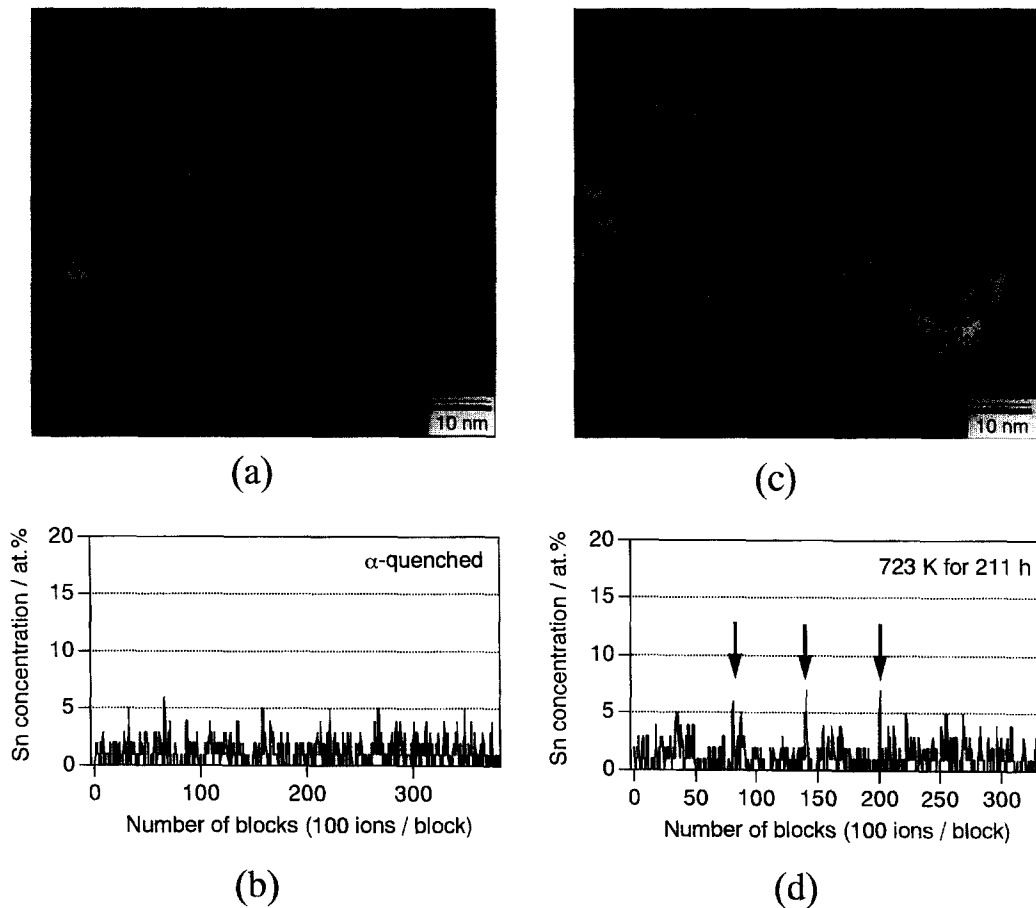

(a)

(c)

(b)

(d)

Fig. 7. (a) and (b) A Ne field ion image and a concentration depth profile, respectively, of α-quenched sample D (Zr–1.39Sn), (c) and (d) a Ne field ion image and a concentration depth profile, respectively, of sample D (Zr–1.39Sn) annealed at 723 K for 211 h.

block (bin size) is usually taken as the number of ions covered by the probe hole. In Fig. 7, the block size is assumed to be 100 ions/block since the analyses were made at higher specimen voltage (over 15 kV) compared to the case shown in Fig. 5. A kind of smoothing technique was employed in the calculation that a block was gradually moved with a moving distance of 30 ions. The statistical error of Sn concentration for each block is similarly calculated using Eq. (1). In both the α-quenched state and the annealed state at 723 K for 211 h, no brightly imaging precipitates are observed in the FIM images, and the overall Sn concentrations are determined to be 1.19 ± 0.06 at.% and 1.20 ± 0.06 at.%, respectively. These values are considered to be the same within the statistical error limit. However, the distribution of Sn concentration appears slightly different because concentration spikes reaching to 7 at.% Sn (indicated by arrows) have been detected only in the annealed specimen. Since the projected diameter of the probe hole is about 2 nm, the presence of smaller precipitates or clusters (whose size is less than 2 nm in diameter) may be masked by the matrix contribution (solvent ions in the adjacent matrix region are simultaneously covered with the probe hole). Therefore, the presence of Sn clusters is tested by a mean separation analysis (MSA) [15]. The basic idea of this analysis is to compare the solute distribution experimentally determined by APFIM analyses with the random distribution of solute which is calculated from the mean solute concentration. We check the distance, or separation, between the neighboring solute atoms. For an alloy whose solute concentration is p, a mean separation of solute atoms $\bar{\mu}$ is given by

$$\bar{\mu} = \frac{1 - p}{p}. \tag{2}$$

If we take an experimentally determined separation between ith solute and $(i + 1)$th solute atoms as μ_i, the

experimental variance σ_{exp}^2 is determined by

$$\sigma_{exp}^2 = \frac{\sum \mu_i^2}{N} - \bar{\mu}^2. \tag{3}$$

The estimated variance from the mean solute concentration is given by

$$\sigma_{est}^2 = \frac{1 - p}{p^2}. \tag{4}$$

The difference of the estimated and experimental variances divided by the standard error τ_{est} can be used as a significance parameter S that quantifies the deviation from the random distribution of solute atoms. S is given by

$$S = \frac{\sigma_{exp}^2 - \sigma_{est}^2}{\tau_{est}}. \tag{5}$$

The standard error τ_{est} is defined by

$$\tau_{est} = \sqrt{\frac{q(1 + 6q + q^2)/p^4}{N}}, \tag{6}$$

where $q = 1 - p$. In addition to the comparison of S values, frequency plots of μ_i, yield more information about the clustering tendency of solute atoms.

Fig. 8 is the frequency plot of a separation distance between neighboring Sn atoms and significance values for sample D α-quenched or annealed at 723 K for 211 h. The same raw data, which were converted to the concentration depth profiles in Fig. 7, were analyzed by MSA. For the α-quenched sample, the peak appears at some positive value and the significance value is negative, indicating that the majority of Sn atoms is located separately from their neighboring Sn atoms and virtually there is no deviation from the random distribution. On the other hand, for the sample annealed at 723 K for 211 h, the peak position shifts to smaller value, namely to zero, and the significance value turns to be positive. This strongly indicates that Sn atoms do not distribute randomly any more and
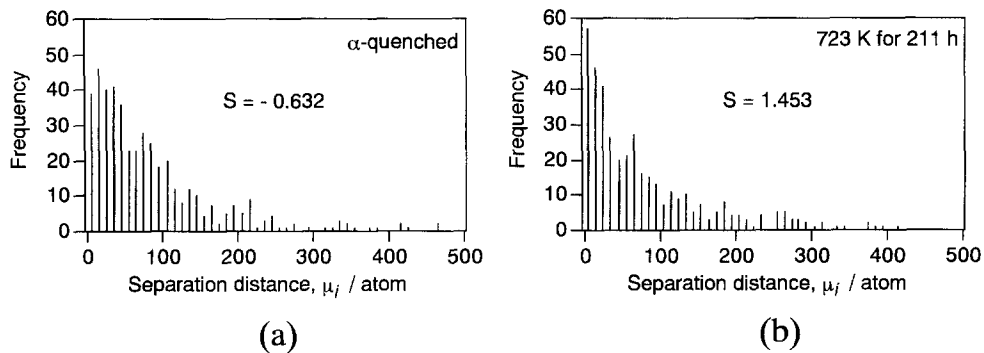

(a)   (b)

Fig. 8. Frequency plots of a separation distance between neighboring Sn atoms and significance values for sample D. (a) and (b) are for specimens α-quenched and annealed at 723 K for 211 h, respectively.
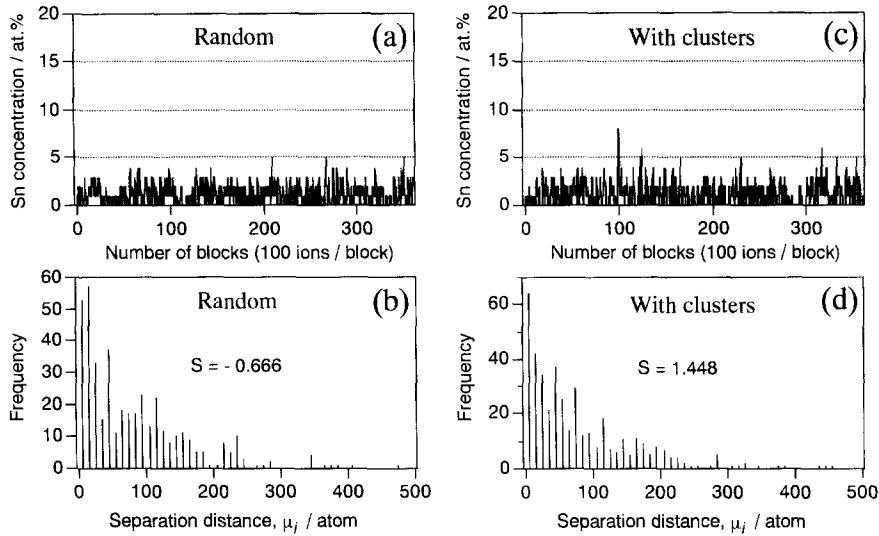
Fig. 9. Simulated concentration depth profiles and their frequency plots of a separation distance between neighboring solute (Sn) atoms. (a), (b) Random solute distribution (dissolved state of Sn), and (c), (d) clusters of Sn are assumed. See text about the selection of parameters for the simulation.

they are located closer with each other, which may be interpreted as the formation of small Sn clusters.

The experimental result shown in Fig. 8 can be compared with simulation. A simulated concentration depth profile, in which small Sn clusters with various size are distributed or Sn atoms dissolve randomly, is generated and then tested by the MSA. Fig. 9 shows a typical simulated concentration depth profiles and their frequency plots of solute (Sn) separation. In this simulation, the total number of ions and mean Sn concentration are assumed to be 35 000 and 1.20 at.%, respectively. Several parameters have been assumed for simulating Sn clusters, such as their size, concentration, number (one-dimensional number density, or what fraction of dissolved Sn atoms is used for making clusters) and location (position in the one-dimensional data chain). In Fig. 9(c), the cluster size is 10 atoms, the Sn concentration of clusters is 50 at.% (a single Sn cluster is composed of 5 solvent and 5 Sn atoms), 5% of Sn atoms in the alloy (0.06 at.% Sn) are used for producing the Sn clusters, and their location is determined by generating random numbers. Since we have used random numbers both for distributing dissolved Sn atoms and for determining the locations of the clusters, the simulated profiles should be treated statistically, therefore, the result shown in Fig. 9 is not deterministic. Actually, sometimes S values were found negative even cluster distributions were assumed. However, more than one hundred trials with the range of the parameters for the clustered state have indicated that the peak of the frequency plots of solute separation appears at the smallest rank μ_1, namely, the separation distance of solute atoms is less than 10 atomic distance. Therefore, it can be concluded that the α-quenched Zr–1.19Sn alloy is different from the alloy annealed at 723

K for 211 h in the Sn distribution in the matrix, and this difference is likely to stem from the formation of the small Sn clusters. Since the S value is a function of μ_i, further simulation studies using various distribution functions for μ_i may be helpful for detecting small solute clusters.

Here, we make a rough estimate of the diffusion coefficient of Sn in α-Zr at 723 K. From Fig. 7(d), the average distance between the Sn clusters can be assumed to be approximately 60 blocks, equivalently about 20 nm (here, one block was taken to be one atomic layer depth). If we take the half of this value as a diffusion distance of Sn at 723 K for 211 h, the diffusion coefficient D can be calculated using $x = \sqrt{Dt}$ as 1.32×10^{-22} m^2/s. This is
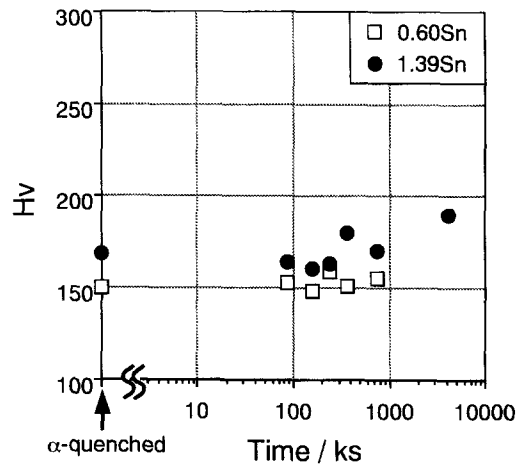

Fig. 10. Micro-Vickers hardness change upon annealing at 723 K for samples C and D.

three orders of magnitude smaller than the previously estimated value using an extrapolated data from higher temperatures over 973 K [14]. This indicates that the diffusion of Sn in α-Zr at lower annealing temperature of 723 K cannot be estimated by only extrapolating from higher temperatures and that the diffusion of Sn in α-Zr at low temperatures is very sluggish.

Finally, the micro-Vickers hardness change of the two binary alloys annealed at 723 K is shown in Fig. 10. The hardness remains almost constant up to 200 h (720 ks), indicating no precipitation hardening occurs. The slight difference of hardness level between two alloys may be due to the difference in Sn concentration in the α-Zr matrix, which appears to contribute to solid solution hardening.

4. Conclusions

We have performed microanalyses of a heat-treated Zircaloy-4, Zr–0.6 wt% Sn and Zr–1.39 wt% Sn alloys using APFIM to clarify as to whether Sn is fully dissolved or not in the α-Zr matrix. It is found that Sn dissolves in the matrix of both Zircaloy-4 and Zr–0.6 wt% Sn alloy upon annealing at 723 K. For the Zr–1.39 wt% Sn alloy, during the annealing for more than 200 h after α-quenching, the symptom of phase separation has been found although no distinct Sn-rich precipitates are detected. The distribution of Sn in the matrix is changed from the α-quenched state, and local regions enriched with Sn, probably small Sn clusters composed of a few tens of atoms, are formed in the matrix.

References

[1] F.H. Froes, T.-L. Yau, H.G. Weidinger, Titanium, zirconium, and hafnium, in structure and properties of nonferrous alloys, in: Materials Science and Technology, K.H. Matucha (Ed.), vol. 8, VCH, Weinheim, 1996.
[2] T.B. Massalski (Ed.), Binary Alloy Phase Diagram, ASM International, Materials Park, OH, 1990.
[3] X. Meng, D.O. Northwood, Microstruct. Sci. 15 (1987) 335.
[4] R. Kuwae, K. Sato, E. Higashinakagawa, J. Kawashima, S. Nakamura, J. Nucl. Mater. 119 (1983) 229.
[5] N.R.V. Bangaru, J. Nucl. Mater. 131 (1985) 280.
[6] J. Aihara, H. Nakamori, H. Kawanishi, Y. Arai, N. Sekimura, S. Iwata, Abstract 117th Mtg. Jpn. Inst. Metals, Honolulu, Hawaii, Dec. 13–15, 1995, Jpn. Inst. Metals, 1995, p. 112.
[7] H.O. Andrén, L. Mattsson, U. Rolander, J. Phys. (Paris) Colloque C2 Suppl. 47 (1986) C2–191.
[8] B. Wadman, H.O. Andrén, U. Rolander, J. Phys. (Paris) Colloque C6 Suppl. 49 (1988) C6–323.
[9] B. Wadman, H.O. Andrén, L.K.L. Falk, J. Phys. (Paris) Colloque C8 Suppl. 50 (1989) C8–303.
[10] B. Wadman, H.O. Andrén, Proc. 8th Int. Symp. on Zirconium in the Nuclear Industry, ASTM-STP 1023 (1989) 423.
[11] B. Wadman, H.O. Andrén, A.L. Nyström, P. Rudling, H. Pettersson, J. Nucl. Mater. 200 (1993) 207.
[12] R.M. Kruger, R.B. Adamson, S.S. Brenner, J. Nucl. Mater. 189 (1992) 193.
[13] N. Sano, Appl. Surf. Sci. 76&77 (1994) 297.
[14] E.A. Brandes (Ed.), Smithells Metals Reference Book, ch. 13, Butterworths, London, 1983.
[15] M.G. Hetherington, M.K. Miller, J. Phys. (Paris) Colloque C6 Suppl. 49 (1988) C6–427.